行政院國家科學委員會專題研究計畫 成果報告

植栽圍籬對低層建築風力通風之影響－非均一孔隙率之探討
研究成果報告(精簡版)

計 畫 類 別 ：個別型
計 畫 編 號 ：NSC 97-2410-H-216-007-
執 行 期 間 ：97 年 08 月 01 日至 98 年 07 月 31 日
執 行 單 位 ：中華大學景觀建築學系

計 畫 主 持 人 ：張瑋如

報 告 附 件 ：出席國際會議研究心得報告及發表論文

處 理 方 式 ：本計畫可公開查詢

中 華 民 國 98 年 10 月 28 日

中國機械工程學刊第三十卷第五期第409~417頁(民國九十八年)
Journal of the Chinese Society of Mechanical Engineers, Vol.30, No.5, pp.409~417 (2009)

Modulation of Cross Ventilation in a Residential Building Using a Porous Hedge

Wei Ru Chang* and Cheng Li Cheng**

Keywords ： *Passive control, Porous hedge, Cross ventilation, Porosity*

ABSTRACT

The present paper has performed a three-dimensional numerical model to study the cross ventilation in a residential building. Examined are the effects of porous hedge placed ahead of the building, and focused are the physical procedures governing air movement during the cross ventilation. The ratio of the space between the hedge and the building to the hedge height is fixed at L/h=2.0, while the hedge porosity is varied from η=0 to 1.0. Detailed information about the mean velocity, pressure, and turbulent kinetic energy is provided to illustrate how the porous hedge affects the cross ventilation in a building of two-side openings. It is found that the porous hedge could modify the mean and turbulent flow structures behind it, and thus alter the cross ventilation of the building. Three types of cross ventilation can be characterized from the results presented, i.e., backward cross ventilation, null ventilation, and forward cross ventilation, respectively. Results further show that the distribution of volume-averaged turbulent kinetic energy has a local minimum value at about the null ventilation conditions.

Paper Received July, 2008. Revised February, 2009, Accepted April, 2009. Author for Correspondence: W.R. Chang

* *Assistant Professor, Department of Landscape Architecture, Fu Jen Catholic University, Taipei County, 24205, Taiwan, R.O.C., Email: rubyweiru@gmail.com,*

** *Professor, Department of Architecture, National Taiwan University of Science and Technology, Taipei 106,Taiwan ROC.*

INTRODUCTION

In a naturally ventilated building, the indoor air is renewed with the outdoor air using wind and/or buoyancy forces. The passive scheme not only improves indoor air quality and thermal comfort [1, 2] but also, when applied properly, leads to a significant reduction of energy consumption in ventilating the buildings [3]. Most importantly, it can avoid the Sick Building Syndrome caused by poor design of active ventilation systems. The combination of the above merits establishes the natural ventilation as the best solution for improving the microenvironment. Consequently, the study of natural ventilation has gained more and more attention in recent years [1-5].

In a typical cross-ventilated building, wind-pressure differences along the facade create a natural air exchange between indoor and outdoor spaces. The ventilation rate depends on the strength and direction of wind forces and the resistance of the airflow path [6]. Direct introduction of outdoor air by wind forces, however, does not necessarily ensure a comfortable indoor environment because it gives no control over undesirable airflow patterns. If the cross ventilation of a building is poorly designed, even with an plenty of wind resources, the period during which windows can be left open is often limited due to uncomfortable wind intrusion. To control wind-driven airflow patterns and thus improving the indoor microclimate, a passive scheme using windbreaks such as forests, nets, and hedges has been employed to modify the cross-ventilation in a building [7]. The porous hedges act not only a shelter from a strong wind [8, 9] but also a regulator to channel airflow properly to ventilate a building. The objective of the present work is to extend the author's 2-D work [7] to develop a 3-D numerical model to study the cross ventilation in a building that are controlled passively by using a porous hedge.

A successful design of wind-driven cross ventilation requires the detailed information of airflow and pressure distributions in and around buildings. The physical processes of wind-driven cross ventilation are

complex, and predicting the ventilation rates is difficult. Although full-scale measurements for a building site can provide reliable data, the experiment is time consuming and hard to control. In addition, the discrete data are not informative enough. In most cases, the experimental data obtained from one building site may not be extended to another because of different weather data and building surroundings [5]. An alternative approach to study the cross ventilation in buildings is the computational fluid dynamics (CFD) technique. The CFD technique is becoming popular due to its informative results and low labor and equipment costs. In the present study three-dimensional CFD model is developed to study the cross ventilation in a building that are controlled passively by using a porous hedge. The effect of the hedge porosity on the airflow characteristics in and around a residential building is examined. The phenomena of cross ventilation in the building are discussed from the detailed distributions of mean fluid flow, turbulent kinetic energy, and pressure distributions. The computational procedure, adopted for the evaluation of such a three-dimensional turbulent flow, is based on the solution of the governing equations for the dependent variables (such as three velocity components, the pressure and the turbulent kinetic energy) by means of the finite volume technique [10, 11]. The airflow is assumed to be steady and turbulent, which is described through the well-known k- ε turbulence model. It has been proven to be able to simulate quite well the mean flow and turbulent kinetic energy of a long, porous hedge standing on flat ground [12-14]. In addition, the k- ε model has an advantage of saving computing time, and thus has become the most widely used CFD method in many industrial applications. This is the reason why the model is employed in the present paper in resolving the problem mentioned above.

THE MODEL

A schematic drawing illustrating the airflow around a residential building along with a porous hedge is shown in Fig. 1. The origin of the coordinate system is set at the rear edge of the porous hedge. The airflow is from left to right. The porous hedge of height h is placed ahead of the building. The distance between the front edge of the building and the rear edge of the porous hedge is 2h (L). The dimensions of the interior space of the building are 2h by 3h by h (length by width by height). The windward and leeward walls have a window of size 0.5h by h. Both windows are open that allows of cross ventilation in the building.

Governing equations The airflow studied is considered as three-dimensional, steady, isothermal, incompressible and turbulent. The fundamental equations governing the motion of the above flow are the averaged Navier-Stokes equations, and the continuity equation, which can be expressed as:

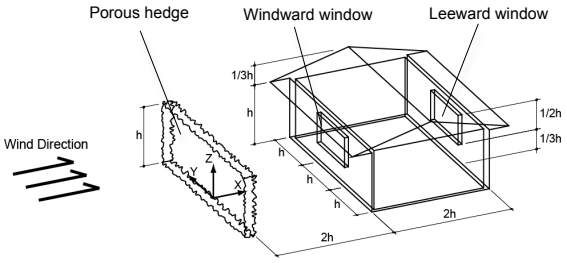

Figure 1 Schematic drawing of the wind-driven cross ventilation around the building.

$$\frac{\partial U_i}{\partial x_i} = 0 \tag{1}$$

$$\frac{\partial}{\partial x_i}\left(U_i U_j\right) = -\frac{1}{\rho}\frac{\partial p}{\partial x_i} + \frac{\partial}{\partial x_i}\left(2\nu S_{ij} - \overline{u_i u_j}\right) \tag{2}$$

$$S_{ij} = \frac{1}{2}\left(\frac{\partial U_i}{\partial x_j} + \frac{\partial U_j}{\partial x_i}\right) \tag{3}$$

The turbulent fluxes of momentum ($\overline{u_i u_j}$) are important terms that govern the turbulent diffusion and need to be specified by certain turbulence models in order to fulfill the closure of the equation set. A number of turbulence models, ranging from simple algebraic models to second-moment closure models, have been developed in the past decades. For simplicity, the standard *k*- ε model is used in closing the equation set. The correlation between the mean turbulent kinetic energy *k* and the dissipation rate of turbulence ε is expressed by the following equations:

$$\overline{u_i u_j} = -2\nu_t S_{ij} + \frac{2}{3}k\delta_{ij} \tag{4}$$

$$\nu_t = \frac{C_\mu k^2}{\varepsilon} \tag{5}$$

where ν_t is the turbulent diffusivity, and δ_{ij} the Kronecker symbol. The transport equations for *k* and ε are

$$\frac{\partial}{\partial x_j}\left(U_j k\right) = \frac{\partial}{\partial x_j}\left[\left(\nu + \frac{\nu_t}{\sigma_k}\right)\frac{\partial k}{\partial x_j}\right] + 2\nu_t S_{ij}\frac{\partial U_i}{\partial x_j} - \varepsilon \tag{6}$$

$$\frac{\partial}{\partial x_j}\left(U_j \varepsilon\right) = \frac{\partial}{\partial x_j}\left[\left(\nu + \frac{\nu_t}{\sigma_k}\right)\frac{\partial \varepsilon}{\partial x_j}\right] + 2C_{\varepsilon 1}\nu_t S_{ij}\frac{\varepsilon}{k}\frac{\partial U_i}{\partial x_j} - C_{\varepsilon 2}\frac{\varepsilon^2}{k} \tag{7}$$

The model constants are also the standard values for wind-tunnel flows:
C_μ=0.09, $C_{\varepsilon 1}$=1.44, $C_{\varepsilon 2}$=1.92, σ_k=1.0, and σ_ε=1.3 [15]

The Darcy's law describes the flow momentum within the porous hedge, i.e.,

$$\frac{\partial}{\partial x_i}(\eta U_i U_j) = -\frac{\eta}{\rho}\frac{\partial p}{\partial x_i} + \frac{\partial}{\partial x_i}(2\eta\nu S_{ij}) - \frac{\eta^2\nu}{\kappa}U_i \qquad (8)$$

where η is the porosity of the hedge, representing the volume occupied by the pores, to the total volume of the porous solid. The permeability κ is a quantity of the surface area to volume ratio of the porous matrix. The last term in the above equation represents the Darcy's drag imposed by the pore walls on the fluid within the pores, and usually results in a significant pressure drop across the porous solid.

Grid creation and boundary As shown in Fig. 2, a half-sphere computational domain is employed to simulate the fluid flow characteristics around the hedge and building. In general, the fluid flow around the building and the porous hedge is changed significantly. Therefore, a fine mesh of high spatial resolution is created around these regions so that an accuracy prediction may be obtained. A total of 1,376,900 unstructured control cells are generated from the whole computational domain. Additional runs for a coarser mesh (1,590,000 cells) and a finer mesh (1,000,000 cells) are obtained by checking grid independence. A comparison of the results of the 1,376,900-cell mesh and the 1,590,000-cell mesh shows that the maximum discrepancy in the mean velocity profiles is 0.05 percent. This change is so small that the accuracy of the solutions on a 1,376,900-cell mesh is already satisfactory.

At the inlet of the computational domain (the upstream quarter sphere), a uniform velocity is imposed. At the downstream section (the downstream quarter sphere), the averaged pressure is chosen as the reference pressure. There is no standard method for setting the turbulence kinetic energy and the dissipation rate in the free stream. In the present simulation, we assume 0.5% turbulence intensity in the free stream. Thus, k and ε at the inlet section can be calculated. All solid boundaries, such as ground and building walls, we use non-slip conditions in conjunction with the wall functions.

The solution method In the simulation processes, the highly coupled, nonlinear, partial differential equations are discretized into a set of linear algebraic equations by using the finite volume discretization method [16-18]. Then, they are solved by iterative solutions on each control cell, defined over the computational domain. A balance between source terms, convention and momentum fluxes is evaluated by the continuity equation at the faces of each cell. The estimation of diffusion fluxes at the cell faces is obtained by a centered approximation, while the first order upwind approximation is adopted for the advection terms. The pressure-velocity linkage is solved via the SIMPLER algorithm [19].

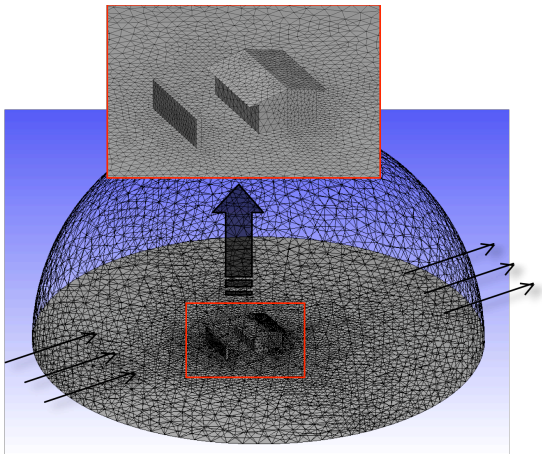

Figure 2 Mesh distributions on the computational domain.

RESULTS AND DISCUSSION

Verification of the model Before the subsequent discussion about the computational results, it is important to validate present numerical procedure and data by comparing the present results with those in previous works. Figure 3 shows a comparison of mean velocity ratios in x (U/U_h) and z (W/U_h) directions between the present predictions and the previous experiments [12]. In this plot, the hedge porosity is fixed at η=0.7, and the axial station selected for comparison is at h/2 behind the hedge. It is seen that both the experimental and simulated results reveal a forward velocity behind the hedge, meaning that there is no flow recirculation. Moreover, both results show a rather uniform distribution of U/U_h for $0.1<z/h<0.9$, where the maximum discrepancy is less than 10%. In the previous experiments, however, a large variation of U/U_h and W/U_h occurs at the elevation $0.9<z/h<1.0$, where turbulence is significant due to the strong shear flow. In general, the above comparisons are satisfactory to confirm that the present numerical procedure is adequate and the present numerical results reliable.

Detailed fluid flow A comparison of mean-flow patterns around the building between the hedge-free case and the solid-hedge case is shown in Figs. 4 and 5.

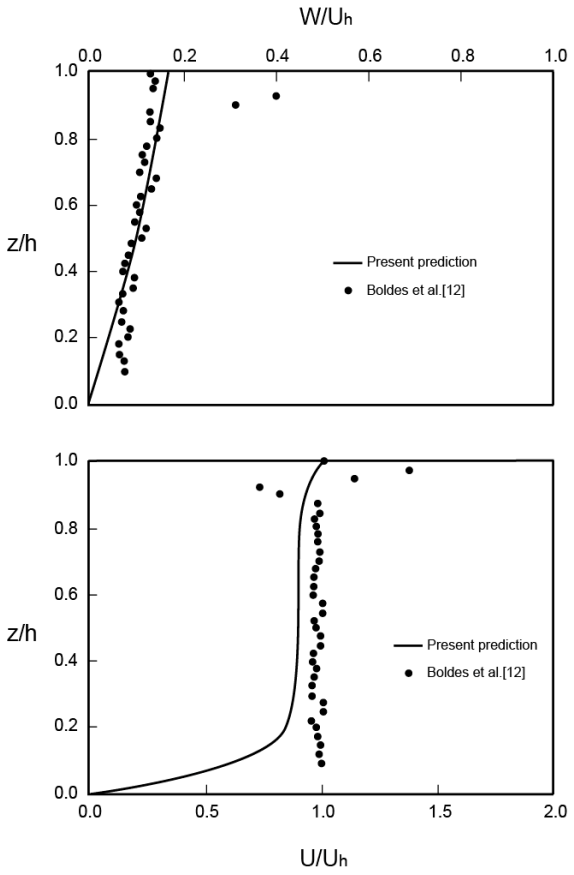

Figure 3 Comparison of the present predictions with previous works.

Figure 4 distributes the mean-velocity vectors on the planes cutting across the middle of the computational module (y=0), whereas Fig. 5 visualizes the mean-flow traces around the building. Figures 4 (a) and 5 (a) are the hedge-free cases, while Fig. 4 (b) and 5 (b) are the results that the solid-hedge is placed ahead of the building. The above results serve as a reference to examine the effect of porous hedge on the cross ventilation in the building.

It is seen from Fig. 4 (a) that the hedge-free case has a forward airflow that ventilates the building as it traverses through a sudden contracting and expanding channel. When a solid hedge stands ahead of the building (Fig. 4 (b)), the airflow is deflected significantly when it approaches the solid hedge, and then separates from the upstream salient of the solid hedge. The relatively low pressure behind the solid hedge (will be shown later) induces the airflow upstream. It thus forms a flow recirculation behind the solid hedge that ventilates the building reversely, with a backward airflow from the leeward window to the windward window.

A particle trace is helpful in visualizing the mean-flow structures in a flow domain. It represents well the trajectory of a massless particle moving in a fluid. In Fig. 5, four particles are released at points of (x, y, z) = (6, 0, 2.75), (-1, 0, 2.75), (-1, 4, 1.5), and (-1, -4, 1.5), respectively, and then move through the flow domain. Each trace is shown by a curve together with the velocity vectors. The color mapping is also provided to illustrate the velocity magnitude along the trace. It is seen from these figures that the trace #1 of the hedge-free case penetrates the building directly from the windward window to the leeward window. In contrast, the trace #1 of the solid-hedge case circulates the particle round the building. It enters the building from the leeward window, then exits from the building via the windward window, and finally turns upward and moves downstream over the building roof. Traces #3 and 4 of the hedge-free case impinge on the front wall of the building directly, while those of the solid-hedge case are deflected by the solid hedge and pass the building laterally.

As the discussion of Figs. 4 and 5, the flow structure around the building is strongly affected by the solid hedge. Therefore, before discussing the effect of porous hedge on the ventilated airflow in the building, it is important to understand the mean velocity distribution ahead of the building, which is regarded as the inlet/outlet conditions of the ventilated building. Figure 6 shows the effect of the hedge porosity on the axial velocity (U) at the mid-station (x/h=1.0) between the porous hedge and the building on the symmetric plane of the computational module (y=0). It is seen that due to the blockage effect, the axial velocity decreases with decreasing the hedge porosity from η =1.0 to 0.4. At η = 0.2, a part of airflow moves upstream indicating that a flow reversal exits behind the porous hedge, which is like that of solid hedge (η = 0).

Focus is now put on the effect of porous hedge on the cross ventilation in the building. Figure 7 compares the distributions of mean-velocity vectors on the plane cutting across the middle of the computational module (y=0) of various hedge porosities, i.e., η = 0.2, 0.4, 0.6 and 0.8. The corresponding pressure distributions on the plane are also provided in Fig. 8. Obviously, the cross ventilation resulting from these four porosities are quite different. At the highest porosity of η = 0.8 (Figs. 7 (a) and 8(a)), the high pressures near the windward window results in a strong airflow into the building. It traverses directly through the building like that of the hedge-free case (Fig. 4 (a)). When the porosity decreases to η =0.6 (Fig. 7 (b)), the strength of forward ventilated airflow is reduced due to a higher blockage of the porous hedge (Fig. 6). Meanwhile, the pressure difference between two windows is lessened (Fig. 8

(a) Hedge-free case

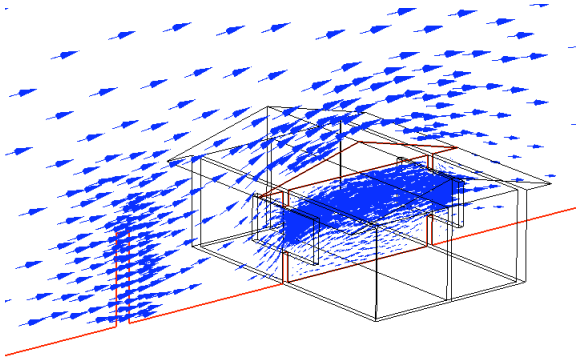

(b) Solid-hedge case (η=0)

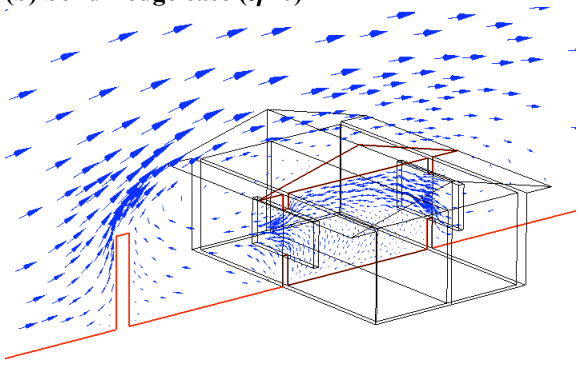

Figure 4 Comparison of mean-flow velocity vectors at the sectional plane cutting across the middle of the computational domain (y=0).

(a) Hedge-free case

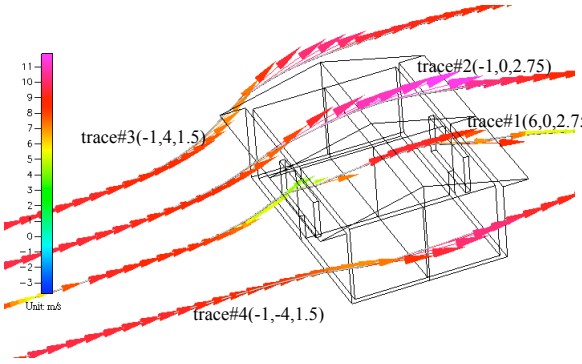

(b) Solid-hedge case (η=0)

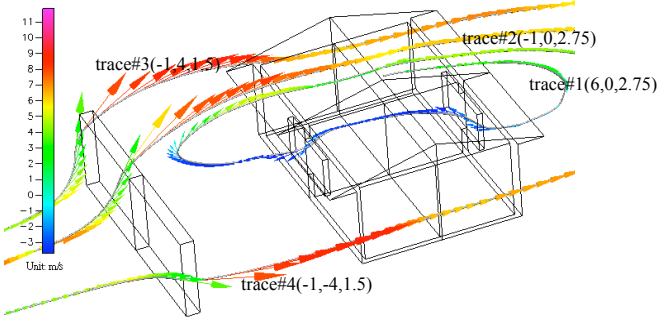

Figure 5 Particle traces around the building for the hedge-free and solid-hedge cases.

(b)). As the hedge porosity further decreases to η =0.4 (Fig. 7 (c)), clearly, the indoor airflow is stagnant almost and the indoor pressures are rather uniform (Fig. 8 (c)). At the lowest hedge porosity of η = 0.2 (Fig. 7(d)), the backward airflow ventilates the building from the leeward window to the windward windows by the adverse pressure gradient in the building (Fig. 8(d)). It is similar to that of the solid hedge, which is dominated by the flow recirculation (Fig. 5 (b)) behind the solid hedge [20].

Figure 9 further shows the effect of the hedge porosity on the pressure distribution along the elevation of z/h=0.58 on the symmetric plane of the computational module (y=0). The solid and dashed curves represents the results of the solid-hedge (η = 0) and hedge-free (η = 1.0) cases, respectively. It is observed that the pressure for the hedge-free case (dashed curve) increases before encountering the building due to the blockage effect, decreases to a local minimum in the building, then bumps up and down, and finally recovers, after the lowest point, to normal

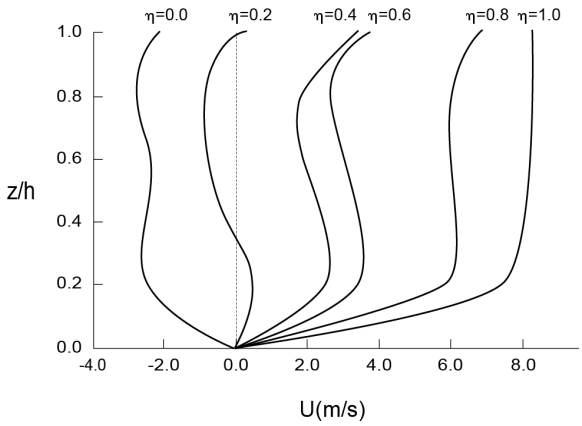

Figure 6 Axial mean velocity (U) distributions at the mid-station (x/h=1.0) between the porous hedge and the building on the module symmetric plane (y=0).

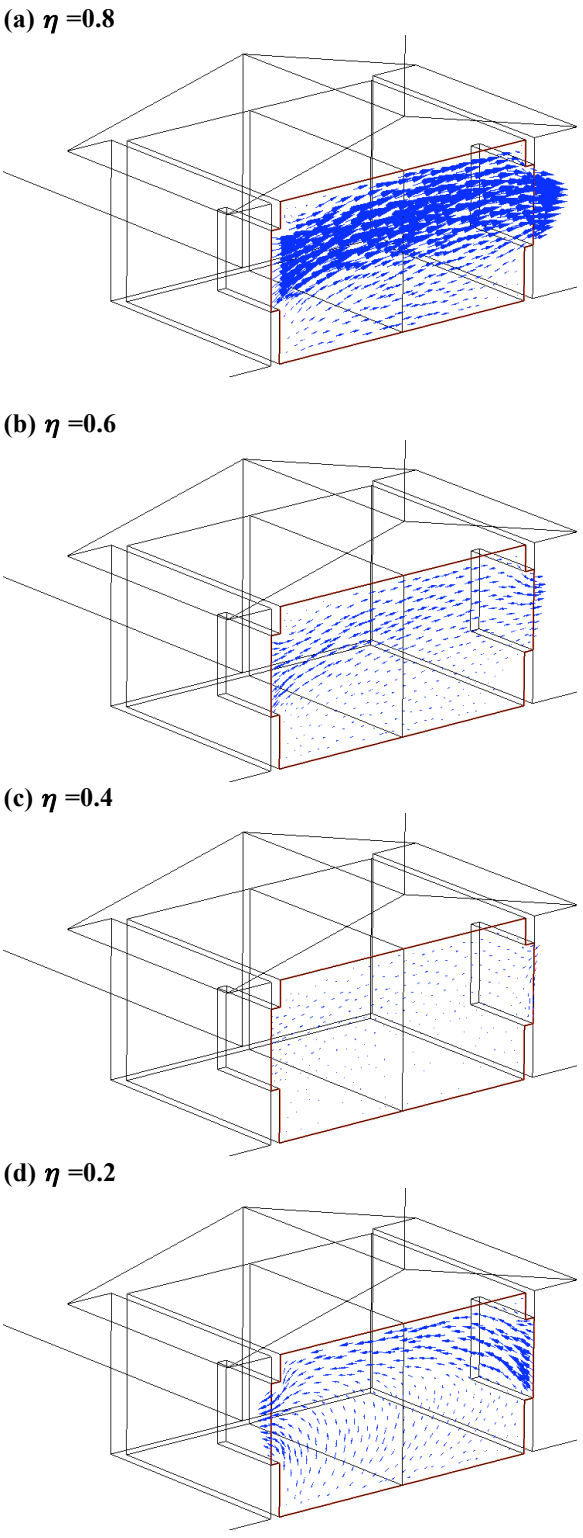

Figure 7 Effect of hedge porosity on the distributions of mean-flow velocities on the mid-plane (y=0) of the building.

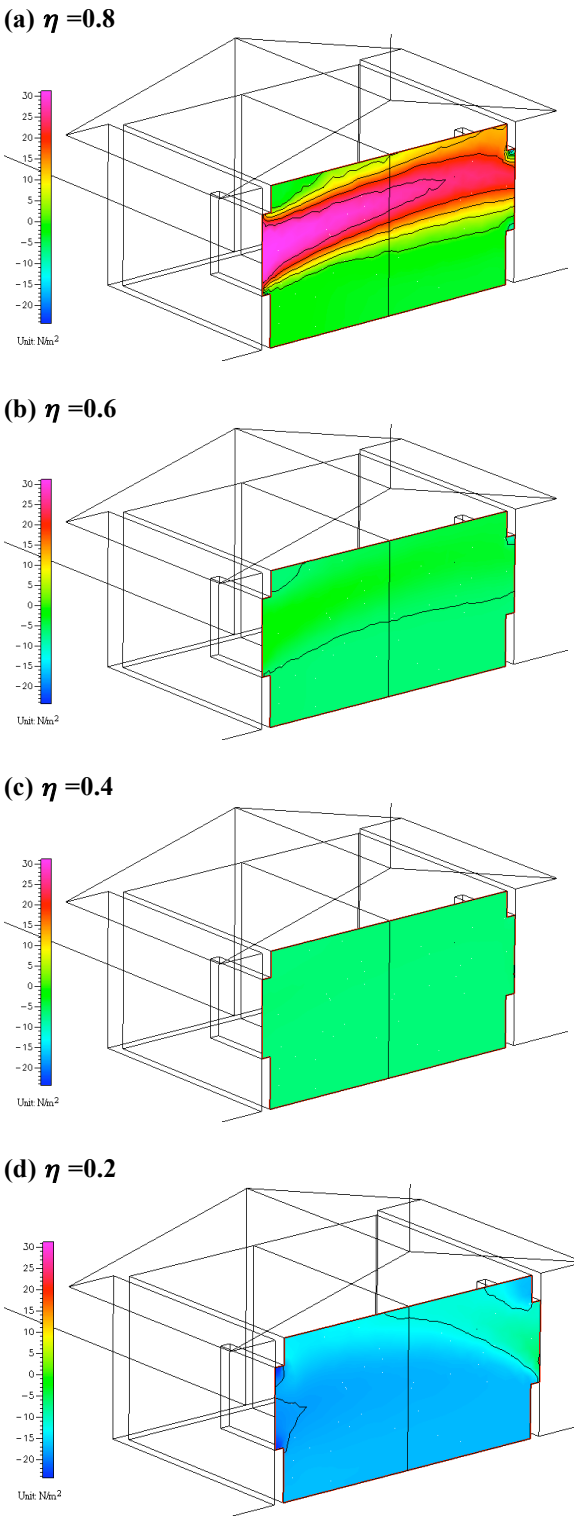

Figure 8 Effect of hedge porosity on the pressure distributions on the mid-plane (y=0) of the building.

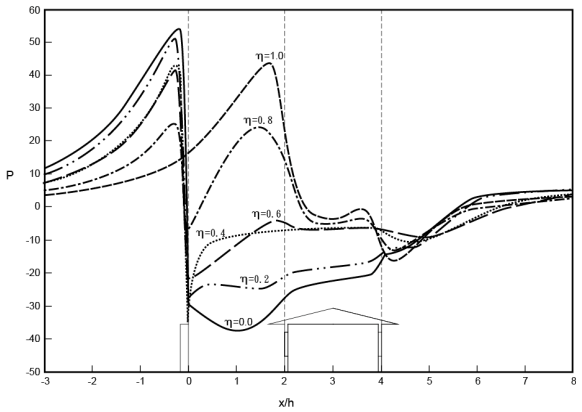

Figure 9 Pressure distributions at the elevation of *z*/h=0.58 along the flow direction on the symmetric plane (*y*=0) of the computational domain.

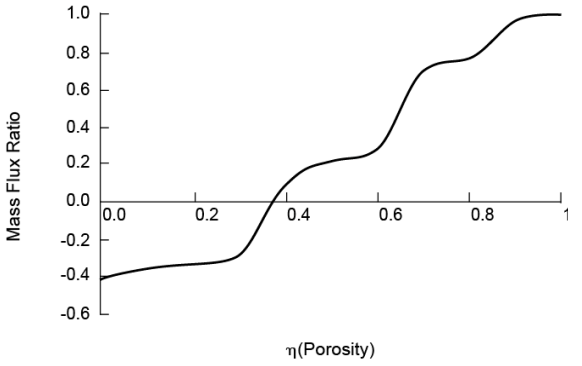

Figure 10 Effect of the hedge porosity on the ventilated airflow rate across the building.

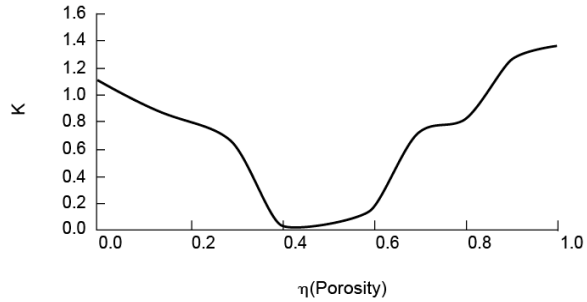

Figure 11 Effect of the hedge porosity on the volume-averaged turbulent kinetic energy in the building.

level. It is further seen that the pressure for the solid-hedge case (solid curve) drops significantly as the airflow across the solid hedge. A relatively low pressure occurs in the region between the solid hedge and the building, which is attributed to the flow reversal [21]. When the porous hedge is placed ahead of the building, the pressures around the hedge and the building are ranged between the solid-hedge case and the hedge-free case. It is interesting to note that the pressures inside the building for $\eta = 0.4$ (dotted line) are rather uniform, meaning that the driving force for the cross ventilation is missing. This confirms the results displayed in Fig. 7 (c) showing a stagnant air inside the build.

It is concluded from the above discussion that the cross ventilation inside the building is strongly affected by the hedge porosity. The ventilation in the building can be characterized by thee categories, i.e., the backward cross ventilation ($\eta = 0.2$), null ventilation (η ~0.4), and the forward cross ventilation ($\eta = 0.6$, and 0.8), respectively.

Ventilated airflow rate Figure 10 shows the effect of porous hedge on the ventilated airflow rate through the building. The abscissa of the plot is the hedge porosity, and the ordinate is the airflow rate ratio between the porous-hedge case and the hedge-free case, i.e.,

$$Se = \frac{\left(\int_A \rho U dA\right)_{\text{with hedge}}}{\left(\int_A \rho U dA\right)_{\text{hedge-free}}} \tag{9}$$

The magnitude of the ventilated airflow rate ratio can represent the shelter effect by the porous hedge. The smaller the absolute value of *Se* is, the higher the shelter effect of the porous hedge becomes. It is seen from Fig. 10 that the ventilated airflow rate ratio becomes negative as the porosity is lower than 0.37. It indicates adverse ventilation from the leeward window to the windward window. After η>0.37, the ventilated airflow rate ratio increases with increasing the hedge porosity. It can be illustrated by the velocity vectors shown in Fig. 7 and the pressure distributions shown in Fig. 8. Therefore, it is concluded that a critical hedge porosity at about $\eta = 0.37$ which results in null ventilation in the building. It is interested to note that the present critical hedge porosity is higher than that obtained for the previous study [7]. This may be attributed to the present 3-D results accounted for the lateral-flow effect that did not consider in the previous 2-D work. Figure 11 further shows the effect of the hedge porosity on the volume-averaged turbulent kinetic energy in the building. The volume-averaged kinetic energy is represented as the following form,

$$\bar{k} = \frac{\int_{\text{vol.}} k dv}{6h^3} \tag{10}$$

It is seen that the value of $\overline{k}$ is high for the both the strong forward ventilation and adverse ventilation. A valley of the curve is found around the null ventilation.

CONCLUDING REMARKS

A three-dimensional numerical model has been performed to examine the effect of porous hedge on the cross ventilation in a residential building. The porosity of the porous hedge is varied from η=0 to 1.0. Results reveal that placing a porous hedge ahead of the building is an effective scheme to modify the cross ventilation by altering the airflow patterns. The cross ventilation inside the building is strongly dependent of hedge porosity. The shelter effect of the porous hedge can be enhanced by decreasing the hedge porosity. An inverse cross-ventilation of the building can be found for low hedge porosity. From the results presented, it can be characterized as the backward cross ventilation for $\eta <$ 0.37, null ventilation for $\eta \sim$ 0.37, and the forward cross ventilation for $\eta >$ 0.37, respectively. Results further show that the distribution of volume-averaged turbulent kinetic energy has a local minimum value at about the null ventilation conditions.

ACKNOWLEDGMENT

This research was sponsored by the National Science Council of Taiwan under contract no. NSC 97-2410-H-216-007.

REFERENCES

[1] Hunt, G.R., Linden, P.F., The fluid mechanics of natural ventilation-displacement ventilation by buoyancy-driven flows assisted by wind, Building and Environment 1999; 34: 707-720.

[2] Aynsley R. Estimating summer wind driven natural ventilation potential for indoor thermal comfort. Journal of Wind Engineering and Industrial Aerodynamics 1999; 83:515–25.

[3] Lu, W.Z., Lo, S.M., Fang, Z., Yuen, K.K., A preliminary investigation of airflow field in designated refuge floor, Building and Environment 2001; 36: 219-230.

[4] Li, Y., Delsante, A., Natural ventilation induced by combined wind and thermal forces, Building and Environment 2001; 36: 59-71.

[5] Chen, Z.D., Li, Y., Buoyancy-driven displacement natural ventilation in a single-zone building with three-level openings, Building and Environment 2002; 37: 295-303.

[6] Chang, W.R., Effect of porous hedge on the cross ventilation in a residential building, Building and Environment, 2006; 41: 549-556.

[7] Hwang, J.J., Dynamic Modeling of a Wind Hydrogen System, Journal of the Chinese Society of Mechanical Engineers, 2009; 30: 221-227.

[8] Hwang, J.J., Liou, T.M., Augmented Heat-Transfer in a Rectangular Channel with Permeable Ribs Mounted on The Wall, Journal of Heat Transfer, 1994; 116: 912-920

[9] Hwang, J.J., Liou, T.M., Heat-Transfer in a Rectangular Channel With Perforated Turbulence Promoters Using Holographic- Interferometry Measurement, International Journal of Heat and Mass Transfer, 1995; 38: 3197-3207

[10] Hwang, J.J., Lai, D.Y., Three-dimensional mixed convection in a rotating multiple-pass square channel, International Journal of Heat and Mass Transfer, 1998; 41: 979-991.

[11] Hwang, J.J., Chen, C.K., Savinell, R.F., Liu, C.C., Wainright, J., A three-dimensional numerical simulation of the transport phenomena in the cathodic side of a PEMFC, Journal of Applied Electrochemistry, 2004; 34: 217-224.

[12] Boldesa, U., Colmana, J., Maranon Di Leo, J., About the penetration of a horizontal axis cylindrical vortex into the nearby downwind region of a vertical porous fence, Journal of Wind Engineering and Industrial Aerodynamics 2003; 91: 859-872.

[13] Packwood, A.R., Flow through porous fences in thick boundary layer: comparisons between laboratory and numerical experiments, Journal of Wind Engineering and Industrial Aerodynamics 2000; 88: 1-24.

[14] Wilson, J.D., Numerical studies of flow through a windbreak, Journal of Wind Engineering and Industrial Aerodynamics 1985; 21: 119-154.

[15] Launder, B.E., Spalding, D.B., The numerical computation of turbulent flow, Computer Methods in Applied Mechanics and Engineering 1974; 3: 269-289.

[16] Hwang, J.J., Chen, P.Y., Heat/Mass Transfer In Porous Electrodes of Fuel Cells, International Journal of Heat and Mass Transfer, 2006; 49: 2315-2327.

[17] Chao C.H., Effect Local Thermal Non-Equilibrium on Porous Electrode In Fuel Cells, Journal of the Chinese Society of Mechanical Engineers, 2007; 28: 275-287.

[18] Hwang, J.J., Full Coverage of Two-Phase Transports In a Porous Electrode of a PEM Fuel Cell, Journal of the Chinese Society of Mechanical Engineers, 2008; 29: 195-205.

[19] Patankar, S.V., Numerical Heat Transfer and Fluid Flow 1980, Hemisphere, Washington, DC.

[20] Hwang, J.J., Liou, T.M., Heat Transfer and

Friction in a Low-Aspect-Ratio Rectangular Channel with Staggered Perforated Ribs on Two Opposite Walls, Journal of Heat Transfer, 1995; 117: 843-850

[21] Hwang, J.J., Cheng, C.S., Augmented Heat Transfer In a Triangular Duct by Using Multiple Swirling Jets, Journal of Heat Transfer, 1999; 121: 683-690.

運用多孔隙圍籬調節住宅建築風力通風之研究

張瑋如
天主教輔仁大學景觀設計學系

鄭政利
國立台灣科技大學建築系

摘 要

本文運用三維數值模型探討兩面開窗住宅建物之風力通風狀況，主要在研究設置於建物前之多孔隙率圍籬對於穿越氣流之影響，包括平均速度、壓力與紊流動能強度之變化。圍籬建物間距離與圍籬高度之比固定為L/H=2.0，而圍籬孔隙率變化為η=0到 1.0。研究結果顯示，多孔隙圍籬會影響穿越建物的氣流結構，進而改變建物室內外的通風型態。本研究歸納出三種典型的通風模式，分別為「逆向通風」、「無通風」，以及「正向通風」。研究亦發現在無通風狀態下體積平均紊流動能強度會達到相對最低值。

行政院國家科學委員會補助國內專家學者出席國際學術會議報告

2009年 7月 31 日

報告人姓名	張瑋如	服務機構及職稱	中華大學景觀建築系 助理教授
會議時間 會議地點	98/07/19~98/07/23 美國舊金山Westin St. Francis飯店	本會核定補助文號	NSC 97-2410-H-216-007
會議名稱	(中文) 第三屆國際永續能源會議 (英文) ASME 3rd International Conference on Energy Sustainability		
發表論文題目	(中文) (英文) Dynamic Modeling Of A Wind Hydrogen System		

1.會議經過

第三屆國際永續能源會議(ASME 3rd International Conference on Energy Sustainability) 於美國舊金山的Westin St. Francis飯店舉行，平行會議有Heat Transfer 2009與InterPACK’2009。 會議時間為98年7月19日至23, 本人於7月月16日出發搭乘華航晚上班機飛往舊金山。

從2006開始每年由美國機械工程師學會(ASME)主辦的國際永續會議，今年是第三屆。 根據大會資料顯示，此次大會有來自全世界三十餘國及地區，總計超過五百人與會。 參與會議的人員有35%是來自工業界與政府機構的R&D人員，而65% 則是來自一般學術或研究機構的研發人員。 從國家來區分，與會人員有58%是來自美國本土，其餘42%則是來自世界各地。

本次大會共安排了兩場聯合會議專題講座 （Joint Conference Keynote Address) 、四場大會專題演講（Energy Sustainability Conference Plenary Address)、以及一場 Yellot Award獲獎者演講 。第一場聯合會議專題講座是由美國國家再生能源實驗室 (National Renewable Energy Laboratory, NREL)主任Dr. Dan Arvizu所主講的“Frontiers of Research in Renewable Energy”，第二場則是GE（General Electric Corporation)資深副總裁 Mr. Mark M. Little所主講的“Advanced Energy Systems and Sustainability”；四場大會專題

演講則是分別由University of Colorado的Professor Moncef Krarti所主講的“Low Energy Heating and Cooling Systems for Buildings”、ACI Services Inc.總裁的Mr. W. Norm Shade所主講的“Efficient Use of Our Natural Gas Resources -An Important Component of Energy Sustainability”、由Chevron Energy Technology Co.資深計畫工程師 Dr. Trevor Demayo所主講的”How Can We Measure Energy System Sustainability?”、以及由University of Minnesota的Professor Jane Davidson 所主講的“Solar After Dark: Storage Options”；而Yellot Award的得主的Professor Aldo Steinfeld (ETH Zurich)的演講題目則是”Fuels from Sunlight, Water, and CO2”。除了上述專題演講外，會場同時有各種潔淨能源設備與相關之量測器材展示，內容相當豐富。

本次會議共計有280篇論文發表，共分成二十五項子題，依論文特性分成21個場次同時進行。本人文章發表時間為第二天（20日）下午 ，約有三十幾人與會聆聽，由於本篇論文是首度完成再生氫能系統動態模擬論文，引起在場與會人員相當大的回響，演講後的討論氣氛極為熱絡，問答不斷，由於時間不足，會後還到場外交換心得、互贈論文，受益匪淺。

2. 與會心得

本會議是因應目前全球發展潔淨能源技術所召開的學術研討會，會場同時來自全世界各先進國家的潔淨能源產品與技術之展示，這種大規模展覽會與研討會結合的方式，是一項趨勢，國內會議也逐漸往這個趨勢發展，參與此次會議受益良多，感觸亦深，最重要的還是要再一次強調學術與產業結合的重要性，台灣的產業要升級一定要有強大的學術研究能力當基礎，否則只是空談，而台灣所召開的學術研討會目前也有與產業密切結合的相同趨勢，兩者互相配合、齊力並進，才能夠提昇台灣科技競爭力 。

最後感謝國科會提供經費補助，使本人能順利參加本會議。

3.考察參觀活動(無是項活動者省略)

無

4.建議

新能源的研發已是必然趨勢，其中燃料電池的應用在國際間即受到相當的重視，建議國內相關環境規劃設計產業亦能投入研發行列

5.攜回資料名稱及內容

(1)2010ASME Heat Transfer與Energy Sustainability徵文通告。
(2)會議手冊乙份。
(3)親自拍攝展覽會照片乙批。

6.其他

無

Proceedings of ES2009
2009 3RD International Conference on Energy Sustainability
July 19-23, 2009, Westin St. Francis, San Francisco, California

ES2009-90221

DYNAMIC MODELING OF A WIND HYDROGEN SYSTEM

J. J. Hwang/Department of Greenergy Technology, National University of Tainan, Taiwan

W.R. Chang/Department of Landscape Architecture, Chung-Hua University, Taiwan

ABSTRACT

Dynamic behaviors of an integrated wind hydrogen system have been modeled mathematically. It is based on a combination of fundamental theories of mechanics, thermodynamics, mass transfer, fluid dynamics, and empirical electrochemical relationships. The model considers wind hydrogen system to be composed of three subsystems, i.e., a wind generator, an electrolyzer, and a hydrogen tank. An additional pressure switch model is presented to visualize the hydrogen storage dynamics under a constant outflow condition. Validation of the wind hydrogen model system is evaluated according to the measured data from the manufacturer's data. Then, using wind power as the primary energy input and hydrogen as energy storage simulated the power system. Finally, flow and electrical characteristics and efficiencies of each subsystem as well as the entire system are presented and discussed. The present model will integrate with fuel cell systems to realize the stand-alone renewable power generator in the future work.

INTRODUCTION

The environmental impact of burning fossil fuels and their inevitable depletion have led to a growing interest in renewable energy sources. These sources of energy can no longer be overlooked, because of the need to achieve sustainable development and compliance with the provisions of the recently enforced Kyoto protocol. Wind energy, for example, is available almost everywhere. It can be harnessed to provide electricity at some of the lowest costs available for new generation [1]. Coupling wind turbines to hydrogen-generating electrolyzers has the potential to provide low-cost, environmentally friendly distributed generation of hydrogen in addition to electricity [2-10]. In this way, hydrogen generation can be a pathway for wind generation to contribute directly to reducing the dependence on fossil fuels. The objective of the present paper is to develop a simulation model that effectively predicts the dynamic behaviors of a wind hydrogen system that comprises subsystems including a wind generator, an electrolyzer, and a hydrogen tank. The integrated model is implemented by using Simplorer simulation platform. The effects of constant hydrogen consumption are examined to demonstrate the transient dynamic behaviors at the standby conditions of a wind hydrogen fuel cell (WHFC) system. It also verifies the effectiveness of the proposed management approach for operation of the integrated wind hydrogen system.

Figure 1 shows a typical wind hydrogen fuel cell system. It consists of a wind generator, a pressurized alkaline electrolyzer for H_2 production, a pressurized tank for H_2 storage, fuel cells for H_2 utilization, a secondary battery bank for electricity energy buffer, and a DC/AC inverter for the user load [11, 12]. Wind generators convert wind energy into electricity. Since the large fluctuations in power are together with the wind energy, a battery bank serves as an instantaneous and daily energy buffer for storing the fluctuating power coming from the wind-power generators. For an electrolyzer, the H_2 generation rate is proportional to the current into the water electrolysis. For space saving and better system performance, H_2 will be produced and stored under high pressure. If neither the wind generator nor the battery can provide sufficient electricity, the fuel cell will utilize H_2 to

produce electricity for the load. The fuel cell needs a DC/DC converter to transform its output voltage level to the DC bus voltage [12, 13]. Since the fuel cell cannot promptly follow a sudden load change and its output voltage changes slowly, it behaves as a constant current/power source. A microprocessor-based controller is used to monitor the status of all wind hydrogen system devices, control and protect them, and coordinate the overall system operation. In the present model, focuses are put on the wind hydrogen subsystem, as shown by a shaded block in Fig. 1. The wind generator supplies electrical energy demand of the electrolyzer for hydrogen production. The hydrogen is then stored in a pressurized tank before needed. A pressure switch ahead of the electrolyzer controls the electrolyzer. When the hydrogen pressure is lower than the set pressure, the pressure switch keeps contact to supply the hydrogen again. If the pressure in the hydrogen tank exceeds the set threshold pressure, the pressure switch cuts off the electrolyzer. In the present simulation, the fuel cell keeps its standby conditions. Thus, a small of amount of hydrogen is consumed by the power requirement of BOPs that reduces the pressure in the H_2 tank. That is the pressure switch is used to control a uniform pressure level in the hydrogen tank.

MODELING

Wind generator model As shown in Fig. 1, the wind generator consists of a squirrel cage induction generator connected to the wind turbine rotor through a gearbox:

- Wind turbine: horizontal axis, three blades, and variable pitch angle.
- Transmission system: gearbox.
- Electric generator: asynchronous generator.

As the wind turbine is placed in an animate air, the amount of power transferred to a wind turbine is directly proportional to the density of the air (ρ), the area swept out by the rotor (A) and the cube of the wind speed (V) [14]:

$$P = \frac{1}{2}\rho C_p A V^3 \tag{1}$$

where C_p is the power coefficient. It is a function of the tip speed ratio and the blade pitch angle for pitch regulated wind turbines. The rotor limits the power extracted from the wind by controlling the blade pitch angle (pitch regulated wind turbine) to decrease the rotor aerodynamic efficiency for high wind speeds and thus limiting the mechanical power extracted from the wind. According to Betz' law, a wind turbine can extract at most 59% of the energy that would otherwise flow through the turbine's cross section, that is C_p can never be higher than 0.59 in the above equation. The tip speed ratio λ is defined as

$$\lambda = \frac{\omega_r R}{V} \tag{2}$$

where ω_r is the angular speed of the rotor blade and R is the blade length. Applying the actuator disk theory [14, 15], the rotor model provides the aerodynamic torque extracted from the wind by the following equation

$$T_w = \frac{P_w}{\omega_r} = \frac{1}{2}\rho A V^2 R \frac{C_p}{\lambda} \tag{3}$$

Usually the rotational speed of the wind turbine is slower than the equivalent rotation speed of the electrical network. Typical rotation speeds for a wind generators are 5-20 rpm while a directly connected machine will have an electrical speed between 750-3600 rpm. Therefore, a gearbox is inserted between the rotor hub and the generator. In the present power systems, the drive train model is usually represented by two masses [16] as shown in Fig. 2. The first mass stands for the wind turbine rotor (blades, hub and low-speed shaft), while the second mass stands for generator rotor (high-speed shaft). The equations of the model are

$$J_r \frac{d\omega_r}{dt} = T_w - T_m \tag{4}$$

$$T_m = D_{mc}(\omega_r - \omega_g) + K_{mc}\int(\omega_r - \omega_g)dt \tag{5}$$

$$T_m - T_g = J_g \frac{d\omega_g}{dt} \tag{6}$$

where K_{mc} and D_{mc} are the stiffness and damping of the mechanical coupling of the drive train, respectively. J_b and J_g are the inertias of the wind turbine blade and generator, respectively. T_m and T_g are the generator mechanical torque and the generator electrical torque, respectively.

The asynchronous machine equations, expressed in a reference frame rotating at synchronous speed and taking positive currents going out from the machine, are [17, 18]:

$$\phi_{ds} = X_s i_{ds} + X_m i_{dr} \tag{7}$$

$$\phi_{qs} = X_s i_{qs} + X_m i_{qr} \tag{8}$$

$$v_{ds} = -R_s i_{ds} + \omega_s \phi_{qs} - \frac{d\phi_{ds}}{dt} \tag{9}$$

$$v_{qs} = -R_s i_{qs} - \omega_s \phi_{ds} - \frac{d\phi_{qs}}{dt} \tag{10}$$

$$\phi_{dr} = X_r i_{dr} + X_m i_{ds} \tag{11}$$

$$\phi_{qr} = X_r i_{qr} + X_m i_{qs} \tag{12}$$

$$0 = -R_r i_{dr} + s\omega_s \phi_{qs} - \frac{d\phi_{dr}}{dt} \tag{13}$$

$$0 = -R_r i_{qr} - s\omega_s \lambda_{dr} - \frac{d\lambda_{qr}}{dt} \tag{14}$$

where the sub-indexes (s, r) stand for the rotor and stator quantities, respectively, and the sub-indexes (d, q) stand for the components aligned with the d-and q-axis in a synchronous rotating reference frame. Variable ϕ represents the flux linkage, v the voltage and i the current. ω_s and ω_g are the synchronous and generator rotor speed, respectively, while s is the slip defined as $s=(\omega_s-\omega_g)/\omega_s$. The electric parameters of the machine, R_s, X_s, X_m, R_r and X_r, stand for the stator resistance and reactance, mutual reactance and rotor resistance and reactance, respectively. All variables are in per unit. The parameters of the wind generator are given in Table 1.

Electrolyzer model The electrolyzer is a crucial part in a wind hydrogen system, and the technical challenge is to make it operate smoothly with intermittent wind energy sources. Most of the R&D on water electrolysis related to renewable hydrogen projects have focused on alkaline systems

now, although there have been some major research efforts on proton exchange membrane (PEM) electrolyzers as well [19-21]. However, the costs associated with PEM-electrolysis are still too high, and the market for small-scale H_2-production units is at present day still relatively small.

An alkaline water electrolyzer consists of several electrolyzer cells connected in series. The electrolyzer model [22-25] considered here is based on the characteristics of individual cells. The calculations of the required operation voltage and the mass flow rates of hydrogen and oxygen are all done on a per cell basis, while the corresponding values for the whole electrolyzer unit are simply found by multiplying by the number of series cells. The equation that describes the behavior of the electrolyzer is:

$$V_{\text{actual}} = V_{\text{OCV}} + \eta_{\text{anode}} + \eta_{\text{cathode}} + \eta_{\text{ohm}} \tag{15}$$

The overpotentials represent here the surplus of electrical voltages necessary to activate the electrode reactions and to overcome the concentration gradients. All of the overpotentials depend on the current density and are calculated by the same manner of the fuel cell. According to Eq. (15), the simplified circuit diagram of an alkaline water electrolyzer cell is displayed in Fig. 3. The following equation expresses the theoretical equilibrium cell voltage V_{OCV} of the alkaline water electrolyzer under the effective working conditions, such as temperature and pressure:

$$V_{\text{OCV}} = V_{\text{o}} + \frac{RT}{2F}\left[\left(\frac{p_{\text{H}_2} - p_{\text{H}_2\text{O}}}{p_{\text{o}}}\right)^{3/2}\left(\frac{p_{\text{H}_2\text{O,r}}}{p_{\text{H}_2\text{O}}}\right)\right] \tag{16}$$

where V_{o} is the reversible cell voltage at standard conditions, p_{H_2}, the operating pressure of hydrogen, and, $p_{\text{H}_2\text{O}}$, the water vapor partial pressure.

The ohmic overpotential can be represented by

$$\eta_{\text{ohm}} = I \times R_{\text{el}} \tag{17}$$

where R_{el} is the internal resistance of the electrolyzer, and given by and:

$$R_{\text{el}} = \frac{d_{\text{e}}}{\sigma_{\text{k}} \times A_{\text{c}}} \tag{18}$$

The electrical conductivity σ_{k} of the electrolyte KOH is given by

$$\begin{aligned}\sigma_{\text{k}} &= 2.62 \times C_{\text{KOH}} + 0.067 C_{\text{KOH}}(T - 273.15) \\ &\quad - 4.8 \times C_{\text{KOH}}^2 - 0.088 \times C_{\text{KOH}}^2 (T - 273.15)\end{aligned} \tag{19}$$

where C_{KOH} is the mass concentration of potassium hydroxide.

According to the partial reactions during the electrolysis of an alkaline solution at the cathode and the anode, the total current density j consists of two parts, the cathodic and anodic parts.

$$j = j_a + j_c \tag{20}$$

The activation overpotentials at the cathode and the anode in the electrolyzer are calculated using the Butler-Volmer equations:

$$j_c = j_{o,c}^{ref}\left[e^{\frac{2\alpha_c F}{RT}\eta_{\text{act,c}}} - e^{\frac{2(1-\alpha_c)F}{RT}\eta_{\text{act,c}}}\right] \tag{21}$$

$$j_a = j_{o,a}^{ref}\left[e^{\frac{2\alpha_a F}{RT}\eta_{\text{act,a}}} - e^{\frac{2(1-\alpha_a)F}{RT}\eta_{\text{act,a}}}\right] \tag{22}$$

The production rates of hydrogen ($\dot{m}_{\text{H}_2}$) and oxygen ($\dot{m}_{\text{O}_2}$) in an electrolyzer cell can be calculated by:

$$\dot{m}_{\text{H}_2} = 2\dot{m}_{\text{O}_2} = N_S \times \varepsilon_F \frac{I}{2F} \tag{23}$$

where ε_F and N_S are the Faraday's efficiency and number of series cells, respectively. The operational parameters for the above electrolyzer are given in Table 2.

Pressure switch model In the present system, a normal closed contact switch is employed to switch the electrolyzer on (signal 0) and off (signal 1) depending on the hydrogen pressure in the tank. For stability, a 2-point regulation method is employed to control the pressure switch. The threshold pressure and its corresponding hysteresis are 500 kPa and 20 kPa, respectively. That is when the hydrogen pressure in the tank exceeds 500 kPa, the electrolyzer is switched off to stop producing hydrogen. If the hydrogen pressure in the tank is lower than 480 kPa, the pressure switch breaks contact to electrolyzer that produces the hydrogen.

Model scheme In this work, a multi-domain simulation program Simplorer is employed to model the wind hydrogen system. It is a quasi-steady simulation tool with a modular structure and can offer a wide variety of algorithms to determine characteristic values, such as average and rms values or rise and fall time during a transient simulation. Besides classic gradient-based algorithms, it also offers a sophisticated genetic optimizer. Conventional manual optimization (trial and error) can handle only a small number of parameter variations and is useful for 2 or 3-dimensional parameter spaces. In contrast, Simplorer can handle higher order problems by using automated optimization algorithm. Therefore, a wide range of influences can be taken into account. In addition, it is composed of linked modules and can be integrated into other simulation programs (e.g., MATLAB Simulink).

RESULTS AND DISCUSSION

Windpower is the only primary power source in the wind hydrogen system. It represents the inlet conditions of the present model. As shown in Fig. 4, two kinds wind dynamics are studied, i.e., uniform wind speeds (Case 1) and hill-like distributions of wind speeds (Case 2).

Figure 5 shows the dynamic behaviors of the electrolyzer and hydrogen tank of Case 1. It is seen that the wind generator with uniform wind speed starts the electrolyzer with constant voltages and currents. The electrolyzer produces the hydrogen that keeps flow rate into the tank at a high level. Meanwhile the the pressure in the hydrogen tank increases linearly due to accumulation of hydrogen. When the hydrogen pressure reaches to 500 kPa, the electrolyzer switched off to stop producing hydrogen. The hydrogen begins flowing out of the tank with a constant flow rate. It is used to provide the auxiliary

power of the standby fuel cell subsystem. Therefore, the hydrogen pressure in the tank decreases gradually. When the hydrogen pressure is reduced to 480 kPa, the electrolyzer is reactive to produce hydrogen again. The slight zigzag of pressure distribution reflects the control strategy of the pressure switch mentioned above, which keeps the pressure in the hydrogen tank in a relatively uniform level, 490 ± 10kPa.

The efficiency of the wind hydrogen system is defined the ratio of hydrogen enthalpy flow to the total windpower across the wind turbine, i.e.,

$$\eta_{WH} = \frac{\dot{m}_{H2} \times h_{H2}}{P_W} \quad (24)$$

Essentially, Eq. (24) can be also represented by the production of the subsystem efficiencies, i.e., wind turbine efficiency η_{tb}, gearbox efficiency η_{gb} asynchronous generator efficiency η_{ag}, AC/DC invertors efficiency $\eta_{ac/dc}$, and water electrolyzer efficiency η_{ZER}. The turbine efficiency is represented by the ratio of the mechanical power delivery by the turbine blades to the windpower input to the wind turbine, while the generator efficiency is defined as the ratio of the shaft work to the produced electrical work. The electrolyzer efficiency is defined as the ratio of the hydrogen production rate to the power requirement of the electrolyzer. Thus, the efficiency of the wind hydrogen system can be represented by

$$\eta_{WH} = \eta_{tb} \times \eta_{gb} \times \eta_{ag} \times \eta_{ac/dc} \times \eta_{EZR} = \frac{\dot{m}_{H2} \times h_{H2}}{P_W} \quad (25)$$

Figure 6 shows the dynamics of the wind hydrogen system efficiency along with some selected subsystem efficiencies for Case 1. Except for the idle conditions, the efficiencies of turbine, generator, and electrolyzer are 43%, 77%, and 58%, respectively. The wind hydrogen system efficiency is about 19% (wind speed 5m/s).

Figures 7 and 8 respectively show the dynamics of the power outs and efficiencies of the wind generator for Case 2. It is seen that the windpower increases sharply with an increase of wind speed since the power contained in the wind is proportional to the cubic of wind speed (Eq. 1). As shown in Fig. 8, after the cut-in wind speed, the turbine efficiency slightly increases and then decreases with increasing wind speed. It has the local minimum at the peak of wind speed distributions. As for the generator, the efficiency slightly increases with increasing the wind speed.

Figure 9 shows the dynamics of the electrolyzer and the hydrogen tank. At the initial stage, the wind is too small to drive the turbine to power the electrolyzer. Therefore, the pressure in the hydrogen tank decreases gradually due to the hydrogen consumption by the standby power requirement of the fuel cell subsystem. When the wind speed increases over the cut-in speed, the generator is active by the windpower and simultaneously the electrolyzer begins to produce hydrogen. The hydrogen pressure in the tank thus increases gradually. A sharp increase in the hydrogen production rate fills up the hydrogen tank quickly. When the pressure reaches to 500 kPa, the electrolyzer is switched off and then the hydrogen pressure in the tank is gradually decreased again. Figure 10 shows the dynamics of the efficiency of the wind hydrogen system. The efficiencies of wind generator and electrolyzer are also included for comparison. Under the active conditions, the efficiency of present wind hydrogen system decreases with increasing ambient windpower, which is ranged from 10% to 14%.

CONCLUSIONS

Exploiting conservation of mass, momentum and energy in a wind hydrogen system has developed a dynamic model in this paper. The majority of the system includes wind generators, an electrolyzer, and a pressured hydrogen tank. Special attention has been given to the modeling of subsystems to clearly quantify the dynamic interactions among each part of the wind hydrogen system. The integrated model is implemented by using Simplorer simulation platform. Case studies of examining the wind-speed effects have demonstrated that the model can capture the transient dynamic behaviors of the wind hydrogen system. It also verifies the effectiveness of the proposed management approach for operation of a stand-alone wind hydrogen system, which is essential for determining control strategy to ensure efficient and reliable operation of each part of the wind hydrogen system. Furthermore, the wind hydrogen dynamic model can be integrated with fuel cell system models to design, analyze and optimize the sustainable energy systems. The extension of this study will be to fully validate the model in our future work.

ACKNOWLEDGMENTS

This research was partly sponsored by the National Science Council of Taiwan under contract no. NSC 95-2212-E-451-002.

REFERENCES

[1] Neville, R.C., "Wind Energy Conversion," Elsevier Science, 1995.

[2] Turner J.A., Sustainable hydrogen production, Science 2004; 305:972–974.

[3] Nowotny J., Sorrell CC, Sheppard LR, Bak T. Wind-hydrogen: environmentally save fuel for the future. Int J Hydrogen Energy, 2005; 30:521–544.

[4] Schucan T.H., Case studies of integrated hydrogen energy systems, Report, IEA/H2/T11/ FR1-2000, International Energy Agency Hydrogen Implementing Agreement Task11- Integrated Systems, Operating agent: National Renewable Energy Laboratory, Golden, Colorado, 1999.

[5] Dutton A.G., Bleijs J.A.M., Dienhart H., Experience in the design, sizing, economics, and implementation of autonomous wind-powered hydrogen production systems, Int J Hydrogen Energy, 2000; 25:705–722.

[6] Stantarelli M., Calı` M., Macagno S., Design and analysis of stand-alone hydrogen energy systems with different renewable sources, Int J Hydrogen Energy, 2004; 29:1571–1586.

[7] Vidueira J.M., Contreras A., Veziroglu T.N., PV autonomous installation to produce hydrogen via

electrolysis, and its use in FC buses, Int J Hydrogen Energy, 2003; 28:927-37.
[8] Peharz G., Dimroth F., Wittstadt U., Wind hydrogen production by water splitting with a conversion efficiency of 18%, Int J Hydrogen Energy, 2007; 32: 3248-3252
[9] Bechrakis D.A., McKeogh E.J., Gallagher P.D., Simulation and operational assessment for a small autonomous wind–hydrogen energy system, Energy Conversion and Management, 2006; 47: 46-59
[10] Iqbal M.T., Modeling and control of a wind fuel cell hybrid energy system, Renewable Energy, 2003; 28: 223-237.
[11] Luque A., Marti A., Increasing the efficiency of ideal wind-power generators by photon induced transitions at intermediate levels, Physical Review Letters, 1997; 78(26): 5014-5017.
[12] Hwang J.J., Wang D.Y., Shih N.C., Lai D.Y., Chen C.K., Development of fuel-cell-powered electric bicycle, J. Power Sources, 2004; 133: 223-228
[13] Hwang J.J., Wang D.Y., Shih N.C., Development of a lightweight fuel cell vehicle, J. Power Sources, 2005; 141:108-115.
[14] Heier, S. Grid Integration of Wind Energy Conversion Systems, John Wiley and Sons, 1998.
[15] Freris L.L., Wind energy conversion systems, Prentice Hall, 1990.
[16] Ledesma P., Usaola J., Rodrı´guez J.L., Transient stability of a fixed speed wind farm, Renewable Energy, 2003; 28: 1341–55
[17] Holdsworth L., Wu X.G., Ekanayake J.B., Jenkins N., Comparison of fixed speed and doubly-fed induction wind turbines during power system disturbances, IEE Proc Gener Transm Distrib, 2003; 150 (3): 343–52
[18] Kundur P., Power system stability and control, New York, McGraw-Hill, 1994.
[19] Wang J.T., Savinell R.F., Simulation studies on the fuel electrode of a H2-polymer electrolyte fuel cell, Electrochimia Acta, 1992; 37(15): 2737-2745.
[20] Yamaguchi M., Shinohara T., Taniguchi H., Nakanori T., Okisawa K., Development of 2500 cm^2 solid polymer electrolyte water electrolyzer in WE-NET, Proceedings of the 12th World Hydrogen Energy Congress, Buenos Aires, 21–26 June 1998. p. 747–55.
[21] Gorgun H., Dynamic modeling of a proton exchange membrane (PEM) electrolyzer, 2006; 31: 29-38.
[22] Gerd Wedler, Lehrbuch der Physikalischen Chemie, Third Edition, VCH Publisher mbH, D-6940 Weinheim (Federal Republic of Germany), 1987.
[23] Carl Hamann, Wolf Vielstich, Elektrochemie, Third revised Edition, WILEY-VCH.
[24] Hartmut Wendt, Electrochemical hydrogen technologies, Electrochemical Production and Combustion of Hydrogen, Elsevier, 1990.
[25] Hans Dieter Baehr, Thermodynamik, Eine Einführung in die Grundlagen und ihre technischen Anwendungen, Ninth Edition, Springer Publisher 1996.

Table 1 Parameters of the Wind generator

Performance	Value	Unit
Air density	1.229	kg/m
Number of blade	3	-
Rotor radius	2.15	m
Start-up wind speed	2.5	m/s
Cut-in wind speed	2.0	m/s
Rated power	50	kW
Rated wind speed	11	m/s
Rated rotor speed	110	rpm
Furling wind speed	12	m/s
Max. design wind speed	60	m/s

Table 2 Parameters and coefficients of the electrolyzer

Parameters	Symbol	Value	Unit
Number of cells	N_s	30	-
Cross section area of the electrolyte	A_c	150	cm^2
Distance between electrodes (Electrode Gap)	d_e	0.0003	cm
Surface factor of electrodes	f_{air}	44.5	-
Cathodic standard exchange current density	$j_{o,c}^{ref}$	0.12×10^{-3}	A/cm^2
Anodic standard exchange current density	$j_{o,a}^{ref}$	0.12×10^{-6}	A/cm^2
Cathodic transfer coefficient	α_c	0.5	-
Anodic transfer coefficient	α_a	0.3	-

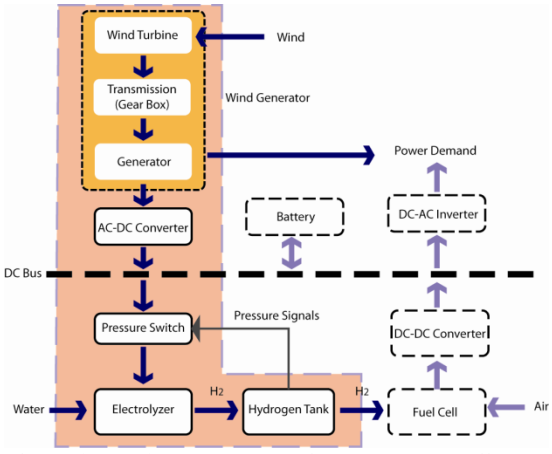

Figure 1 Typical wind hydrogen fuel cell (WHFC) power system.

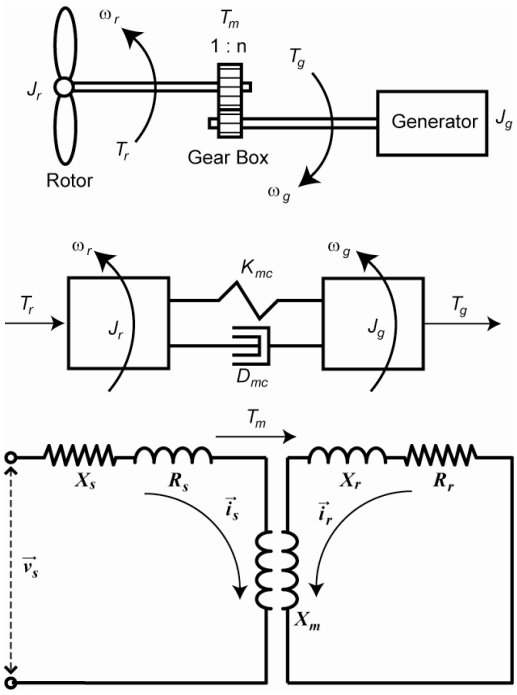

Figure 2 Structure and equilibrium circuit diagram of the wind generator.

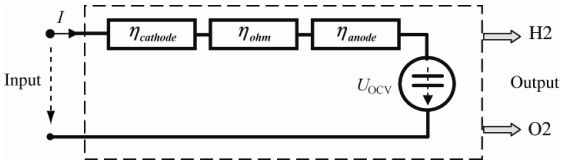

Figure 3 Simplified circuit diagram of the water electrolysis cell.

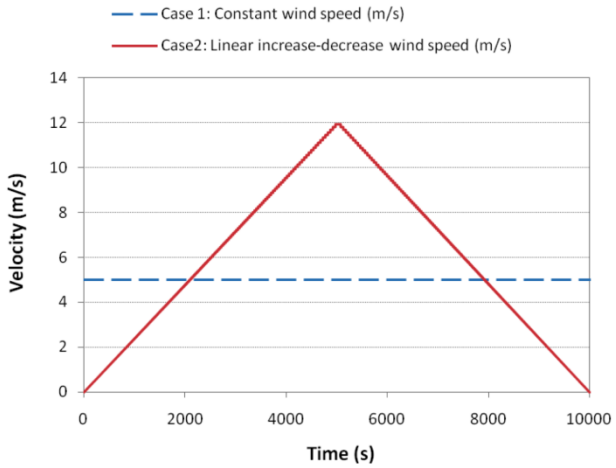

Figure 4 Inlet conditions of the present model, wind dynamics.

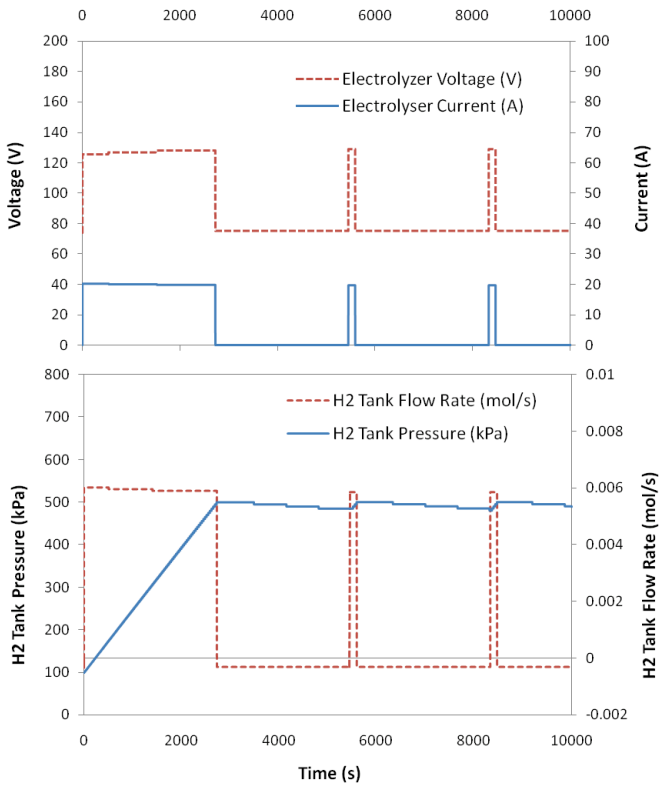

Figure 5 Dynamic behaviors of the electrolyzer and hydrogen tank for Case 1.

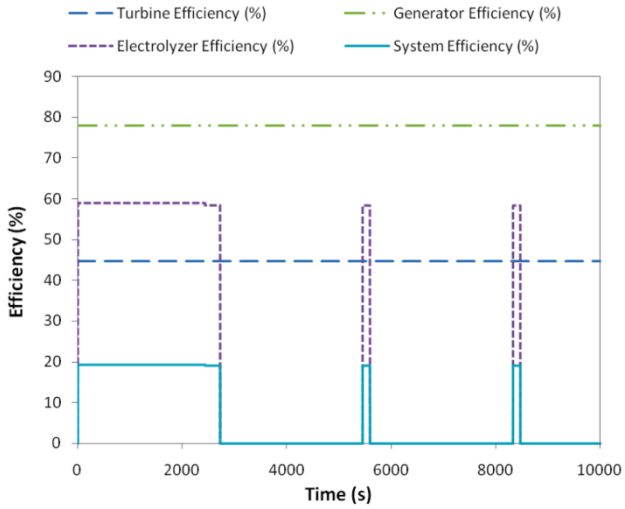

Figure 6 Efficiencies of the subsystems of the wind hydrogen system for Case 1.

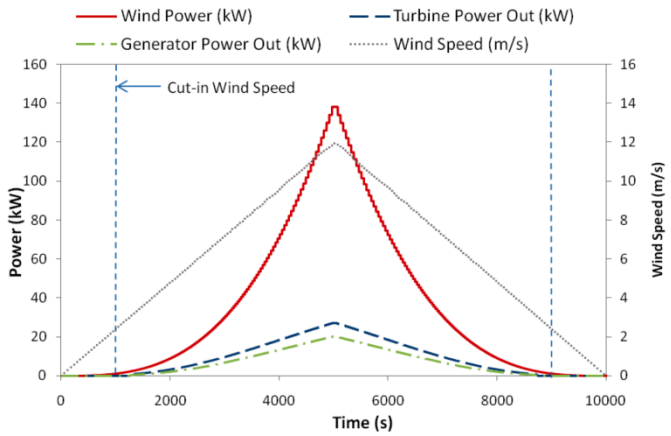

Figure 7 Power deliveries of subsystems of the wind generator for Case 2.

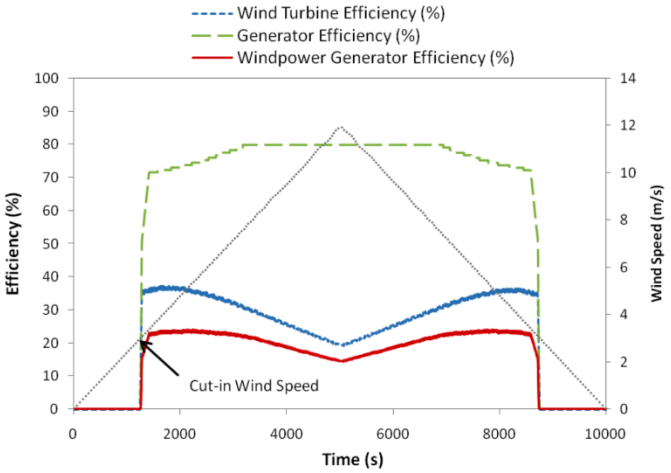

Figure 8 Efficiencies of subsystems of the wind generator for Case 2.

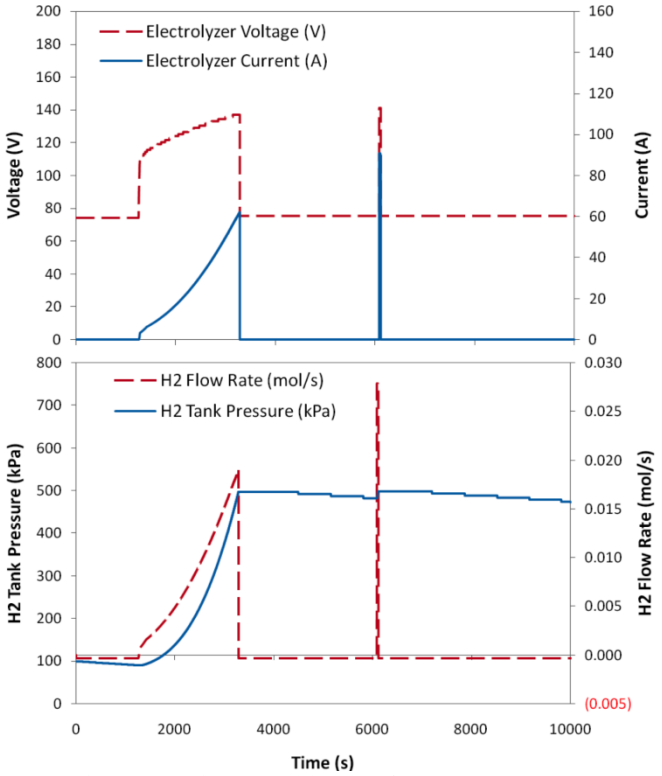

Figure 9 Dynamic behaviors of the electrolyzer and hydrogen tank for Case 2.

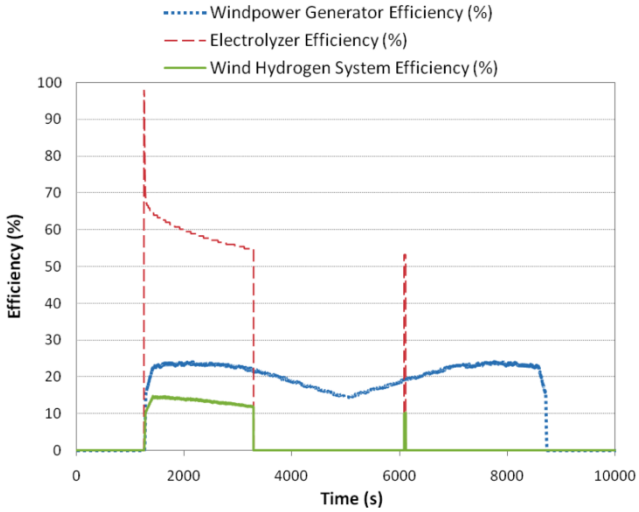

Figure 10 Dynamics of the efficiency of the wind hydrogen system for Case 2.